Hindawi
Geofluids
Volume 2022, Article ID 2534002, 23 pages
https://doi.org/10.1155/2022/2534002

Research Article

Failure Mechanism of Anchored Rock under Constant Resistance Values of Cable Based on Particle Flow Code

Xiaoming Sun,[1,2] Li Cui,[1,2] Yong Zhang,[1,2] Zuoxun Jiang,[1,2] and Lei Wang[1,2]

[1]*State Key Laboratory for Geomechanics and Deep Underground Engineering, China University of Mining and Technology-Beijing, Beijing 100083, China*
[2]*School of Mechanics and Civil Engineering, China University of Mining and Technology-Beijing, Beijing 100083, China*

Correspondence should be addressed to Li Cui; victor__cui@163.com

Received 9 July 2022; Accepted 10 August 2022; Published 28 August 2022

Academic Editor: Wang Yu

Focusing on a constant resistance (CR) cable, using particle flow code (PFC) software, the constant resistance characteristics of the cable are replaced by the servo control of the pallet, and the compressive mechanical properties of rock anchored on the free surface of a tunnel under different constant resistance values (CRVs) are studied. The results show that (1) during the compression failure process of the anchored rock, the stress-strain curve has a "double peak" feature, and the number of cracks has a "step" feature. The mutation point of the number of cracks corresponds to the two peak points of the stress-strain curve. (2) When the constant resistance value of the pallet is approximately 70%-80% of the absolute rigid support strength, the anchored rock has the maximum compressive strength, most stable deformation, maximum pallet energy absorption effect, and minimum number ratio of tensile-shear cracks. The mechanical properties of the CR-anchored rock are the best. (3) According to the different failure forms, the failure types of anchored rock under different CRVs are divided into the overall single-arch collapse type, connected double-arch collapse type, nonconnected double-arch collapse type, and local single-arch collapse type. The research results provide a reference for the design of a CRV and collapse prediction of the anchored surrounding rock.

1. Introduction

Anchor cable is widely used supports in underground engineering [1, 2]. The mechanical properties of anchored and unanchored rocks differ, and the basic properties of rock mechanics are not directly applicable to engineering anchored rock masses. Therefore, research on the mechanical properties of anchored rocks is of substantial practical significance in the design, support, and disaster prevention of rock engineering. Scholars studied the influence of cable parameters on the anchoring effect and obtained the best anchoring parameters [3–5]. Subsequently, researchers have focused on the interaction mechanism between the support and rock masses; established corresponding theoretical models; and considered the influence of factors such as cracks, water, and temperature [6–9]. Notably, the research methods applied to anchored rock are becoming increasingly diversified. The development of acoustic emission damage detection [10], scanning electron microscope (SEM) of rock transparent rock [11], and 3D printing [12] improves understanding of mechanical properties the mechanical properties of traditional anchored rock.

A CR cable was developed to fulfill the support requirements of deep-buried tunnels [13]. The cable's structure is shown in Figure 1 and mainly includes the anchor end, rod body, CR device, pallet, and nut. The CR device is the main structure that deforms. Its principle is that the diameter of the cone is slightly larger than the inner diameter of the sleeve such that the cone receives CR from the sleeve wall during the extraction process. The CRV was approximately 80%-90% of the yield strength of the cable [14]. Next, the element model and the ideal elastic-plastic constitutive

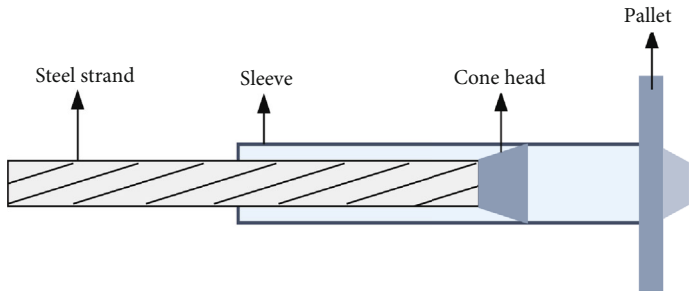

Figure 1: Structure of the CR cable.

relation of the CR cable were proposed (Figures 2 and 3) [15]. Tao conducted a static tensile test, and the obtained test curve is shown in Figure 4, which conforms to the quasi-ideal elastic-plastic constitutive relationship [16]. The two-dimensional elastic-plastic analytical model of the CR cable was extended to three dimensions. Many scholars have used large-scale physical model tests and numerical methods to study the engineering effects of CR cables and produced rich academic achievements [17–21].

Although there are achievements in the literature, the research objects are mainly traditional anchored rock and a single CR cable. Research on CR-anchored rocks has been rare. Because of the wide use of CR cables, research on the mechanical properties of CR-anchored rock is imminent. Scholars [22] have attempted to use the discrete element method to study anchored rock, which proves that the discrete element method has unparalleled advantages in the study of meso-failure mechanisms. Thus, this study combined the engineering background of the large cross-section circular tunnel in Muzhailing to simplify the engineering of anchored rock into numerical samples and used PFC to perform numerical experiments on CR-anchored rock with different CRVs. The aim was to provide a reference for the support design of CR cables.

2. Numerical Experiment Design and Preparation

2.1. Engineering Model. The engineering for this study was the large cross-sectional circular tunnel of Muzhailing, Dingxi City, Gansu Province, China. The rock samples required for the test were obtained from this area. The surrounding rock of the tunnel is mostly soft rock and had large deformation after excavation; therefore, a CR cable was used for support. In this study, an anchored rock unit was the research object. The geometric similarity ratio of the experiment object and the engineering object was determined to be 1 : 10, the size of the numerical model was 50 × 100 mm, and the size of the pallet was 30 mm (Figure 5).

After a tunnel is excavated and supported, it experiences a certain amount of deformation within a certain period, from being a circle with a radius of R to a circle with radius r (Figure 6). Assuming that the convergent value of the tunnel section is uniform, let point a on the section reinforced by the pallet be the research object. Next, within time t,

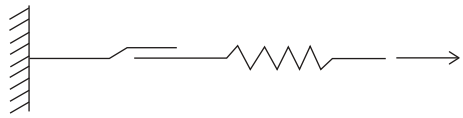

Figure 2: Element model of constitutive relation [15].

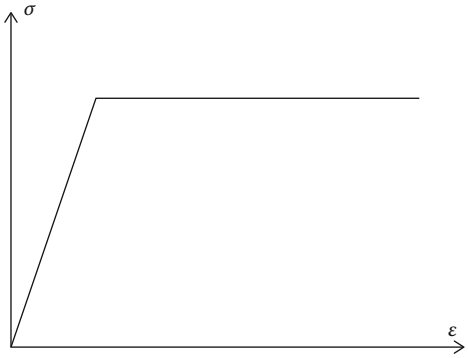

Figure 3: Ideal elastoplastic constitutive relationship [15].

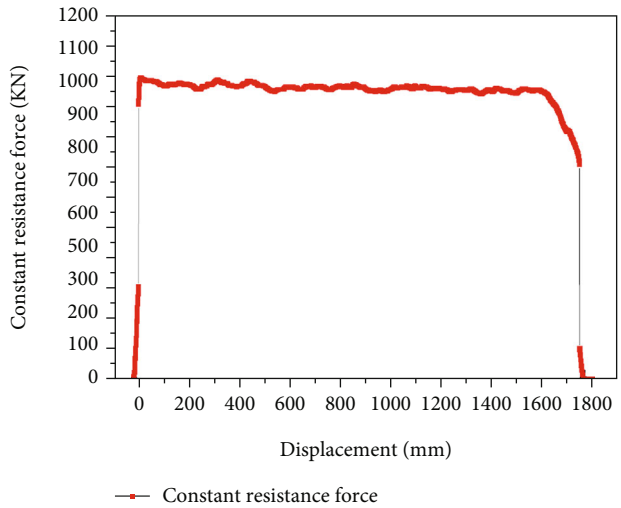

Figure 4: Static tension curve of CR cable [16].

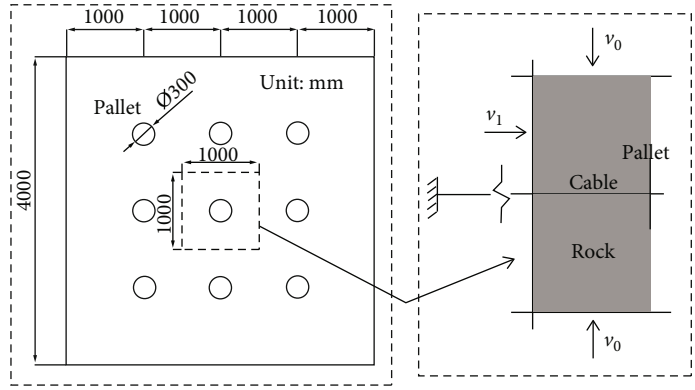

Figure 5: Engineering model and experiment model of CR rock.

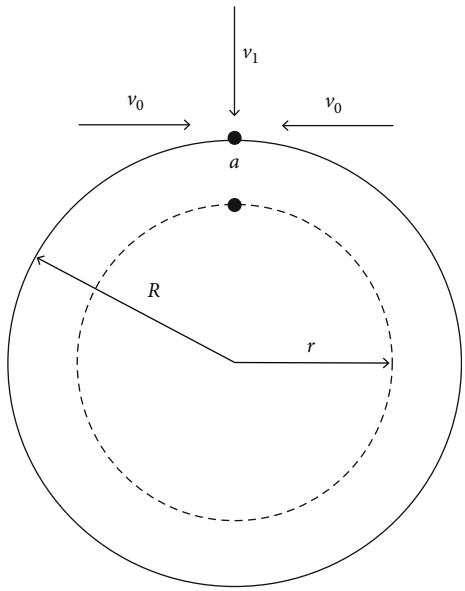

Figure 6: Loading speed at point a during tunnel deformation.

the speed at which point a receives radial pressure from the tunnel section is

$$v_1 = \frac{R - r}{t}. \tag{1}$$

The tangential pressing speed at point a is

$$2v_0 = \frac{2\pi(R - r)}{t}. \tag{2}$$

The ratio of axial and radial loading speed at point a is

$$\frac{2v_0}{v_1} = 2\pi. \tag{3}$$

2.2. PFC Realization Method of CR Properties of Cable. In this study, PFC was used to analyze the failure mechanism of CR rock. The CR cable adopts the method of end anchoring. For the rock mass on the free surface of the roadway, the anchoring effect of the cable is transmitted to the rock mass through the pallet. Therefore, this study ignores the cable and directly performs servo control on the pallet to realize the constant resistance control effect of CR cable. The numerical model and loading method are shown in Figure 7.

The upper and lower walls of the numerical model represent the tangential compression of the tunnel; the left wall represents the radial compression of the tunnel, and the right wall represents the pallet. Equation (3) shows that the ratio of the axial and radial velocities is constant at 2π; therefore, in this paper, the loading speed of the upper and lower walls is $v_1 = 0.01$ m/s, and the loading speed of the left wall is $v_0 = 0.0032$ m/s.

The logic principle whereby the pallet achieves the effect of CR through servo control is shown in Figure 8.

Eleven sets of numerical tests were conducted. First, a rigid anchored rock test without a CR effect was conducted; that is, the pallet did not move during the rock deformation process, and all test termination conditions were set to the compressive strength of the sample to drop to 50% of the peak strength, and the corresponding maximum stress value of the pallet was set to 100% CRV. The other 10 conditions were 0% (without pallet), 10%, 20%, and 90% of the CRV, and the corresponding rock sample numbers were R0, R10, R20, and R100, respectively.

2.3. Parameter Calibration. Among the numerical contact models in the literature, the parallel bond model can better simulate the mechanical properties of rocks. The parallel bond model is similar to that of the cement material between rock particles and has certain tensile, compressive, and shear resistance capabilities. In the case of a fracture, the model can degenerate into a linear bond model [23], and its constitutive relationship is shown in Figure 9.

For calibrating the model parameters, a uniaxial compressive strength experiment was conducted on a mudstone sample collected from an engineering site with a height of 100 mm and a diameter of 50 mm, and its stress-strain curves were obtained. Next, the "elimination method" [25] was used to continuously adjust the parameters so that the

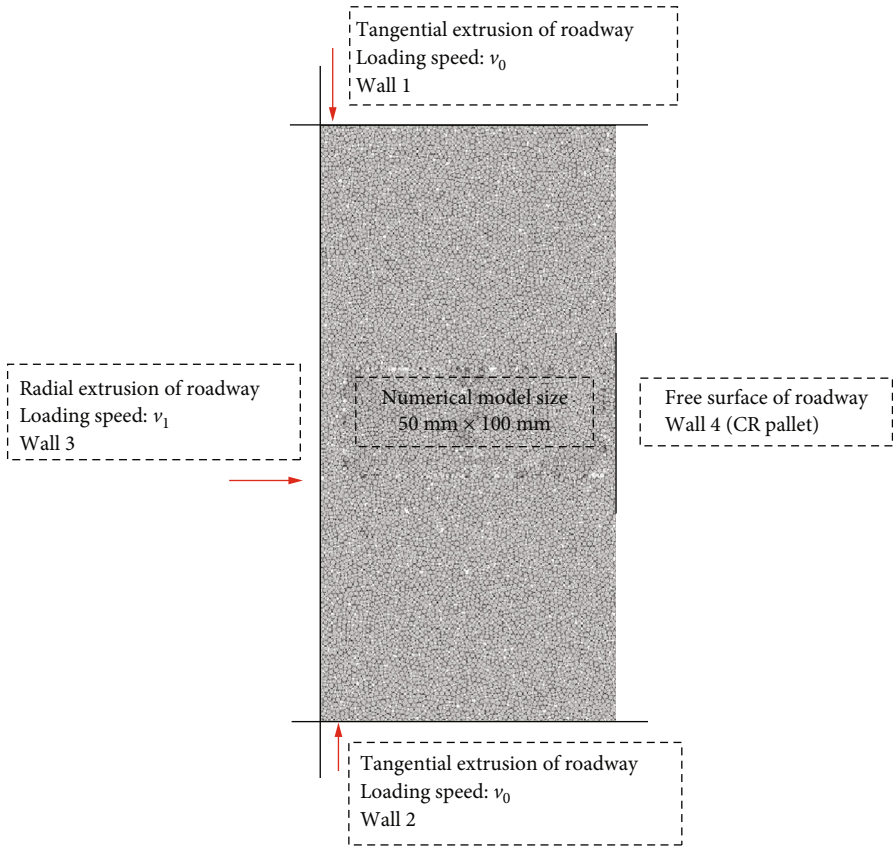

Figure 7: Numerical model and loading method.

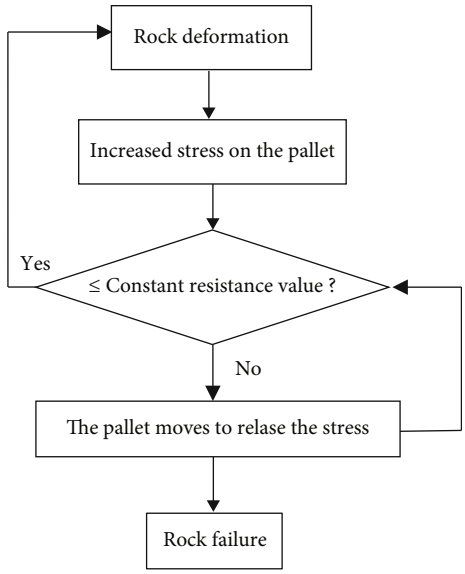

Figure 8: Logic principle of pallet servo control.

stress-strain curve of the numerical experiment was consistent with the stress-strain curve of the physical experiment (Figure 10), and the failure mode of the numerical sample was basically the same as that of the physical experiment (Figure 11). The set of parameters were determined to be the final parameters required for the numerical experiment (Table 1).

3. Strength and Deformation Properties

3.1. Stress-Strain Curve. According to the numerical experiment results, the axial stress-strain curves of the rock samples under different CRVs and the stress pallet with the axial strain of the rock samples were obtained (Figure 12). Among them, the pallet with 100% CRV is an ideal rigid pallet that simulates a rigid cable without displacement, and other percentages of CRVs are based on this. First, according to the stress curve of the pallet, there are constant resistance intervals, and as the CRVs increases, the constant resistance interval continues to decrease until it is 0. The stress curves of most pallets show an obvious ideal elastoplastic constitutive relationship, which indicates that the CR effect of the pallet is reflected. For rock sample R70, the pallet stress exhibited an obvious sudden change in the CR interval. This occurred because the servo control speed of the pallet cannot keep up with the change in speed of the pallet stress, but it still shows a considerable part of the CR effect.

The stress-strain curves of the sample show single peak characteristics when the CRV is 0, 10%, and 100%, and the other cases show obvious double peak characteristics. This result shows that the CR effect of the pallet can change the

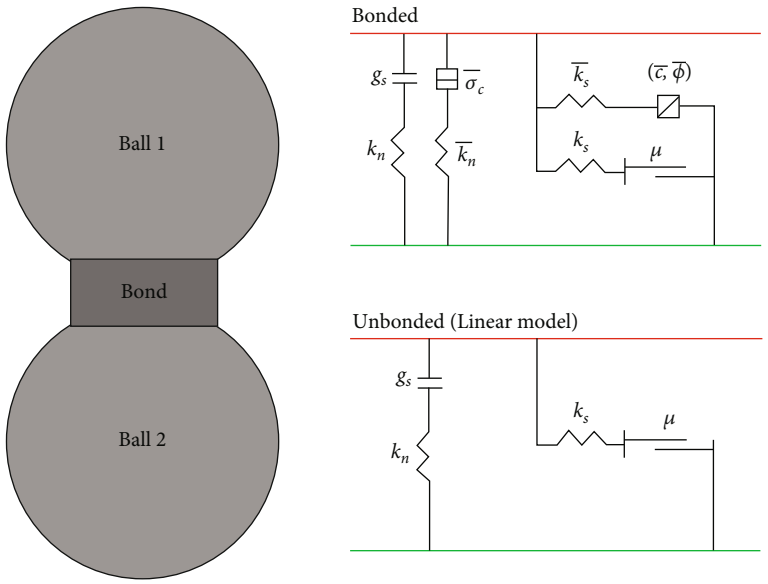

Figure 9: The parallel bond model [24].

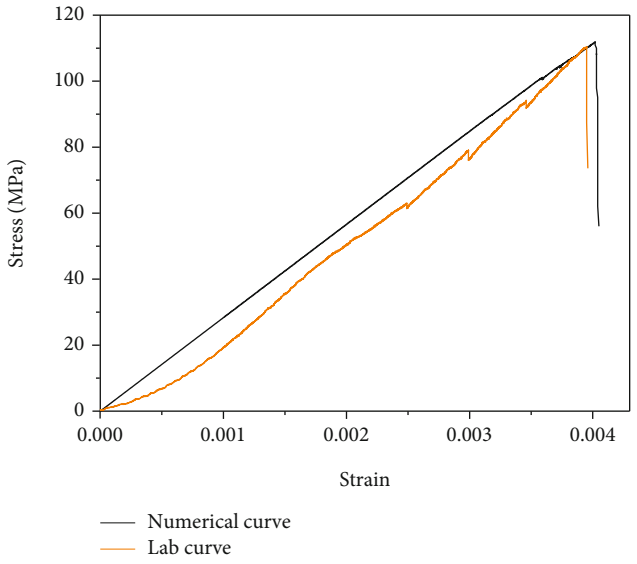

Figure 10: Stress-strain curve.

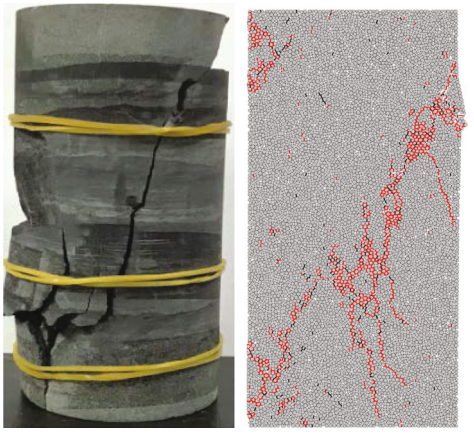

Figure 11: The failure mode.

stress-strain curve from a single peak to a double peak, effectively improving the post-peak strength of the rock. However, if the stress-strain curve has a single peak, the damage is relatively sudden. In the case of a double peak, when the first inflection point appears, the time difference between the two peaks caused by the CR effect can be used to reinforce the rock or evacuate personnel and materials in time, improving the safety of construction.

3.2. Strength and Deformation. Figure 13 shows the strength-CRV curves of the samples. Except for sample R30, the strength increased monotonically with increasing CRV. When the CRV reached approximately 70%, the strength of the sample tended to stabilize and no longer changed significantly. The main reason for the above result is that after the CRV reaches 70%, when the strength of the sample reaches its peak, the pallet stress still does not reach the CRV, and there is no displacement to relieve the pressure; thus, the CRV after 70% does not affect the rock strength. The strain corresponding to the peak stress was called the peak strain, and the strain at the end of the experiment was called the maximum strain. Figure 14 shows the curve of the peak strain versus the CRV. Before the CRV reached 50%, the strain fluctuated significantly, and the deformation became unstable. When it reached 70%, the strain tended to stabilize.

Figure 15 shows the curve of maximum strain versus CRV; when the CRV was 80%, the maximum strain value of the sample reached its maximum. From an energy

Table 1: Numerical parameters of mudstone.

Micro-parameters	Values	Remarks
Minimum radius, R_{min} (mm)	0.3	Parameter of particle
Ratio of maximum to minimum of radius, R_{rat}	1.6	Parameter of particle
Density, ρ (kg/m3)	2700	Parameter of particle
Young's modulus, *Ec* (GPa)	10.0	Parameter of particle
Ratio of normal to shear stiffness, k_n/k_s	0.5	Parameter of particle
Young's modulus of the parallel bond, *Ec* (GPa)	14.5	Parameter of parallel bond
Ratio of normal to shear stiffness of the Parallel bond, k_n/k_s	0.5	Parameter of parallel bond
Tensile strength of the parallel bond, σ_c (MPa)	60	Parameter of parallel bond
Cohesion of the parallel bond, *c* (MPa)	65	Parameter of parallel bond
Friction angle of the parallel bond, ϕ	32	Parameter of parallel bond

perspective, the energy stored inside the rock mass is dissipated more through plastic deformation and pallet displacement, which further reduces the possibility of local rock bursts in the tunnel. Figure 16 shows the curve of the elastic modulus versus the CRV. Before the CRV reached 40%, the elastic modulus of the samples fluctuated significantly. When the CRV reached 70%, the elastic modulus reached its maximum and tended to stabilize.

The aforementioned analysis shows that when the CRV is 70%-80%, the effect is the best, which can not only maximize the strength of the CR-anchored rock but also release the internal strain energy, and the deformation of the rock is relatively stable, which is beneficial to the tunnel stability control of the surrounding rock.

4. Crack Evolution Behavior

4.1. Crack Number Evolution Behavior. The number of the types of cracks can accurately reflect the failure mechanism of the rock. Figure 17 shows the change in the number of cracks. The types of cracks included tensile, shear, and total cracks. There are mutation points in the change in the crack number for all samples. The first mutation point corresponds to the peak strength point, and the second mutation point corresponds to the second peak point of the stress-strain curve, which forms the "Step effect" of the crack number change. Under the action of a CR pallet, the number of cracks will not reach the maximum immediately; however, at the first sudden point, the number of cracks reaches a certain high level quickly and then becomes stable for a period of time. If the sample deformation continues, the number of cracks again reaches the second sudden point. The "step effect" makes the following possible: If many cracks are observed in the surrounding rock for the first time within a short time, individuals can reinforce in a timely manner the surrounding rock or evacuate personnel and materials and make full use of the delay effect of the "step effect" to ensure the safety of life and property before the complete destruction of the surrounding rock.

Rock resists compression and shear but not tension. In Figure 17, after the first mutation point, the number of tension cracks is much larger than the number of shear cracks; thus, the anchored rock mass in the tunnel experiences mainly tension and compression failure, accompanied by partial shear failure. Next, the influence of CRV on the proportion of the types of cracks was investigated; thus, the ratio of tensile and shear crack numbers corresponding to different CRVs was determined (Figure 18).

The ratio decreases as the CRV increases. That is, when the rock was broken, the proportion of tensile cracks continued to decrease, whereas the proportion of shear cracks continued to increase, which was beneficial to the rock. Additionally, a "step effect" in the ratio of tensile-shear cracks was observed to show a downward trend. When the CRV reached 70%, the ratio of tensile and shear cracks entered the lowest interval, indicating the importance of a 70% CRV to anchored rock.

4.2. Crack Shape Evolution Behavior. The evolution of the crack shape can more intuitively reflect the rock failure process than quantity. Figure 19 shows the crack development patterns corresponding to the different CRVs. Red and black indicate the tensile and shear cracks, respectively. The crack state of each sample corresponded to six different axial stress states, which accounted for 100%, 90%, 80%, 70%, 60%, and 50% of the peak stress. When there is no pallet reinforcement, the cracks gradually expand to the middle and rear after generation and then penetrate to the other corner of the free surface, finally forming an overall arc-shaped collapse zone. When the CRV appeared and gradually increased, the distribution of cracks in the middle of the sample gradually decreased. When the CRV reached 30%, the sample cracked from one end of the free surface, and many cracks were concentrated at one end. In the middle of the samples with a low CRV, some scattered cracks remained. When the CRV was high, the cracks in the middle of the sample almost completely disappeared.

The 30% pallet CRV has a critical influence on crack evolution. Before this value, the failure pattern of the free surface was almost completely collapsed. After this value, it mainly collapsed locally, but the rock remained relatively intact. In contrast with the strength control, the pallet can

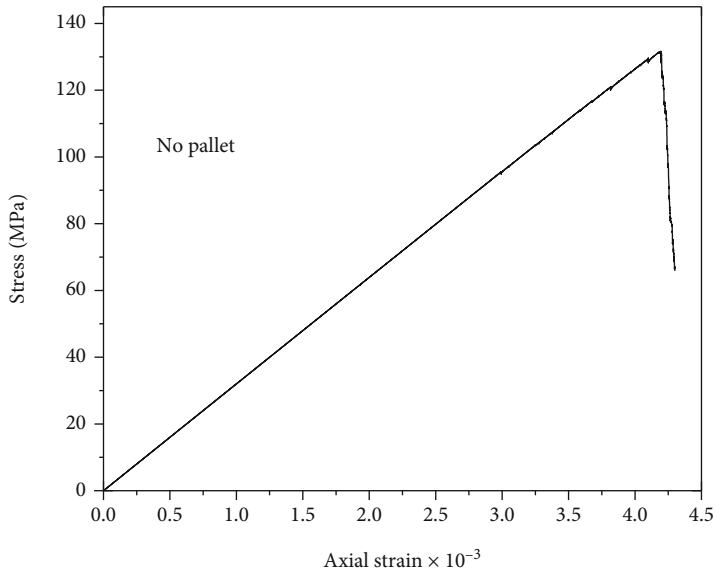

(a) R0

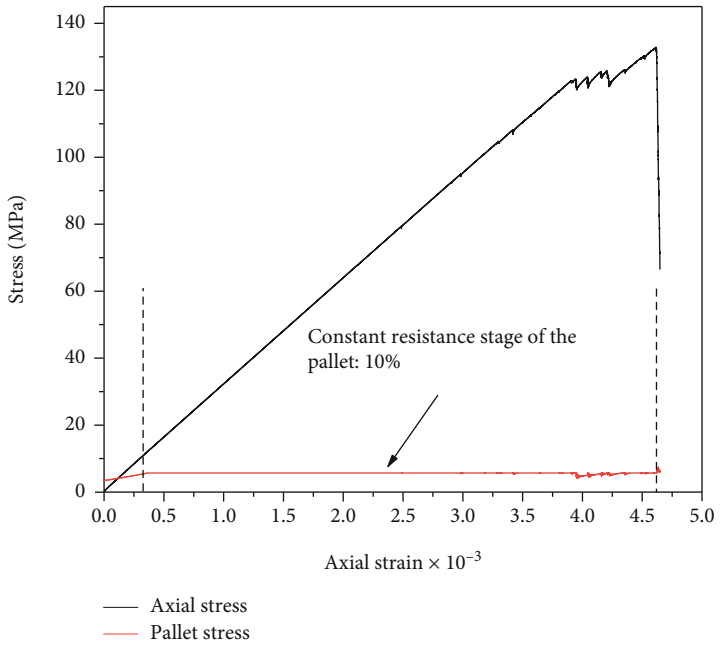

(b) R10

Figure 12: Continued.

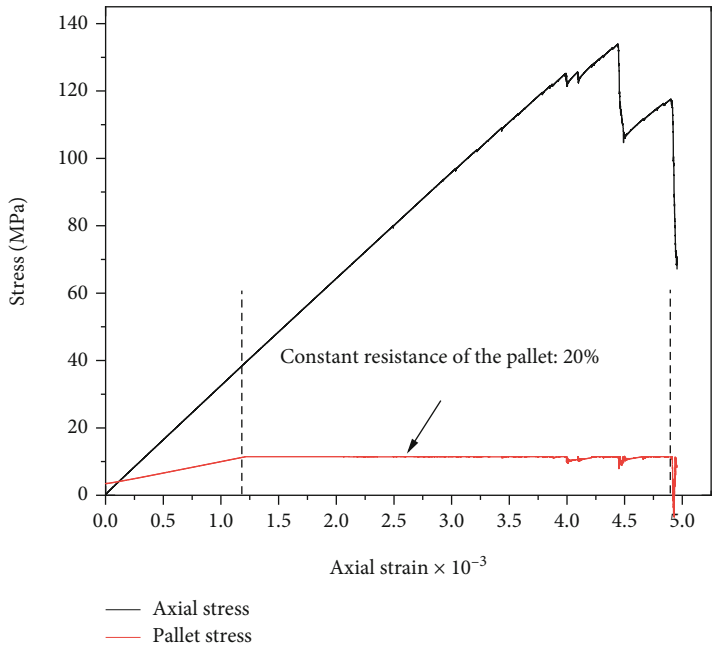

(c) R20

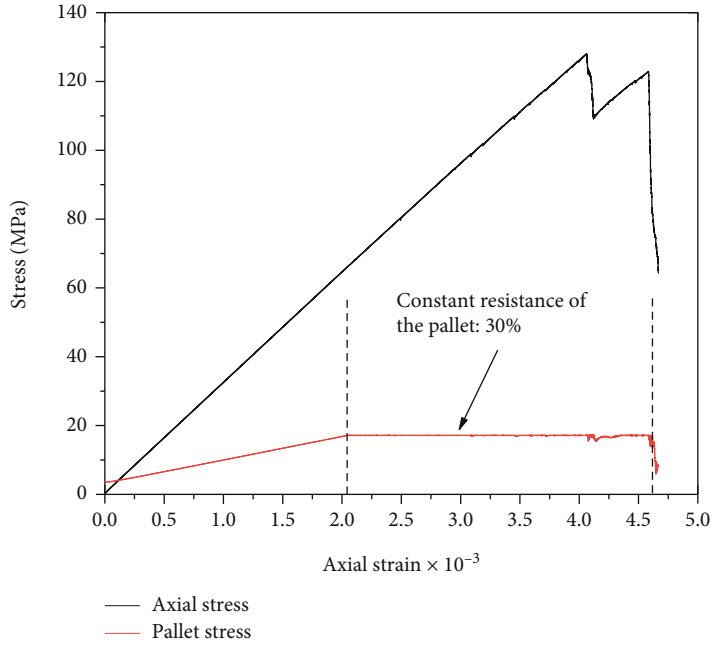

(d) R30

Figure 12: Continued.

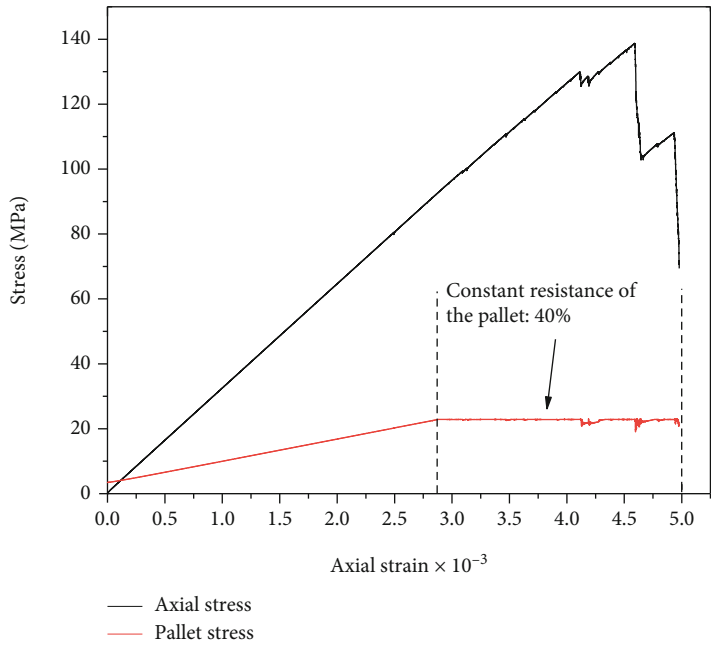

(e) R40

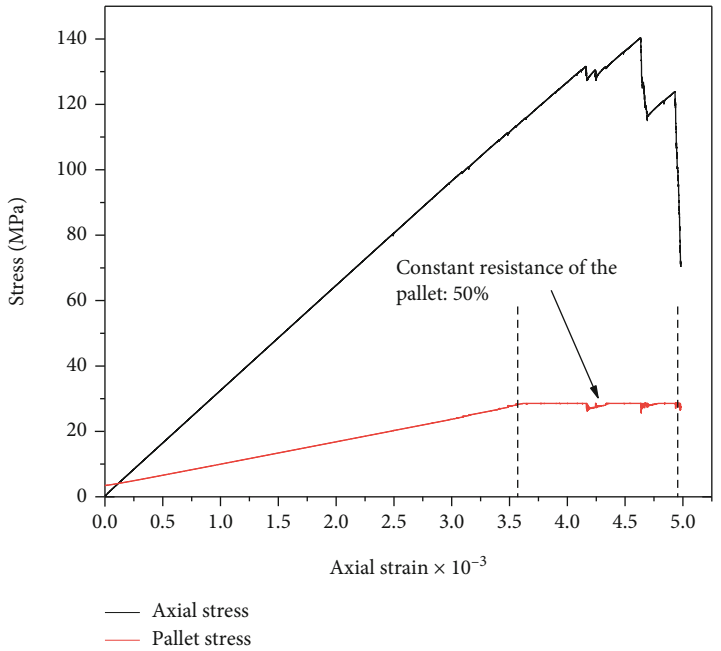

(f) R50

Figure 12: Continued.

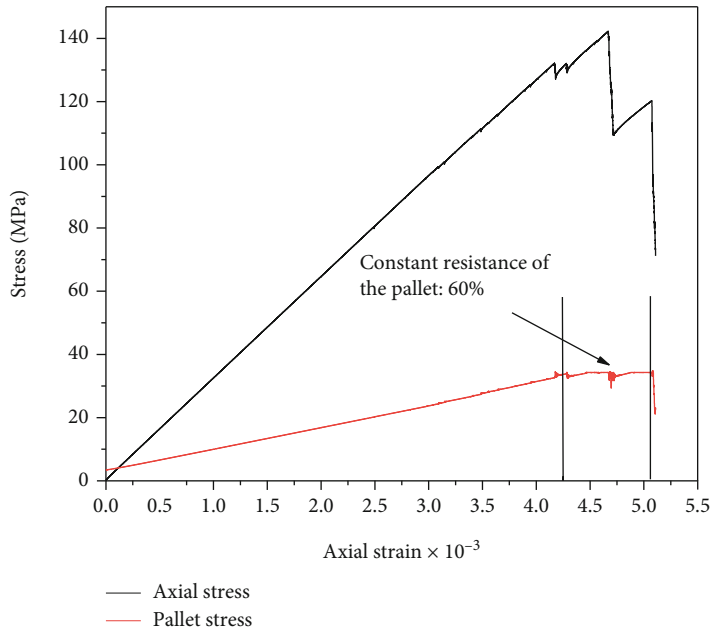

(g) R60

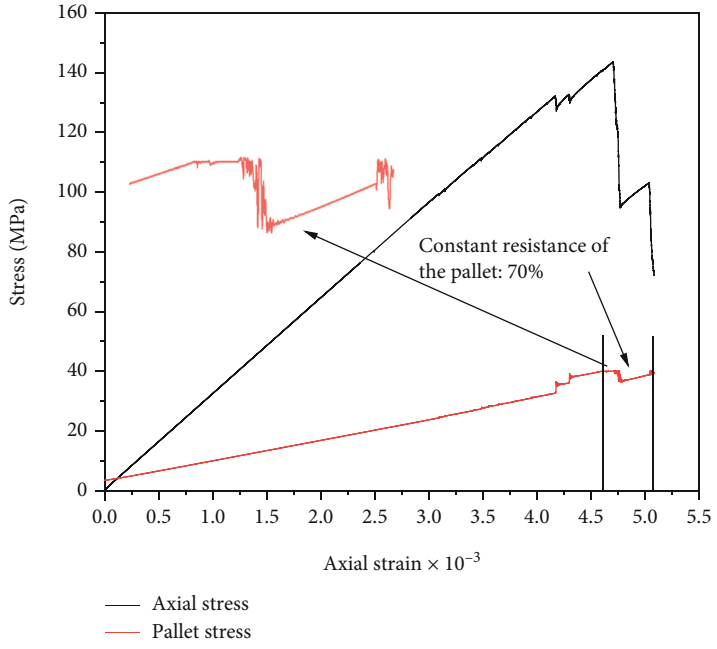

(h) R70

Figure 12: Continued.

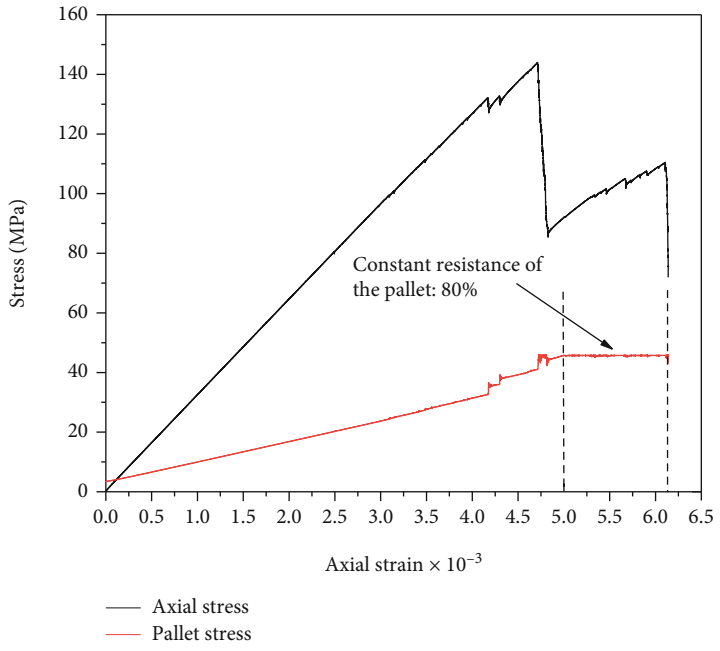

(i) R80

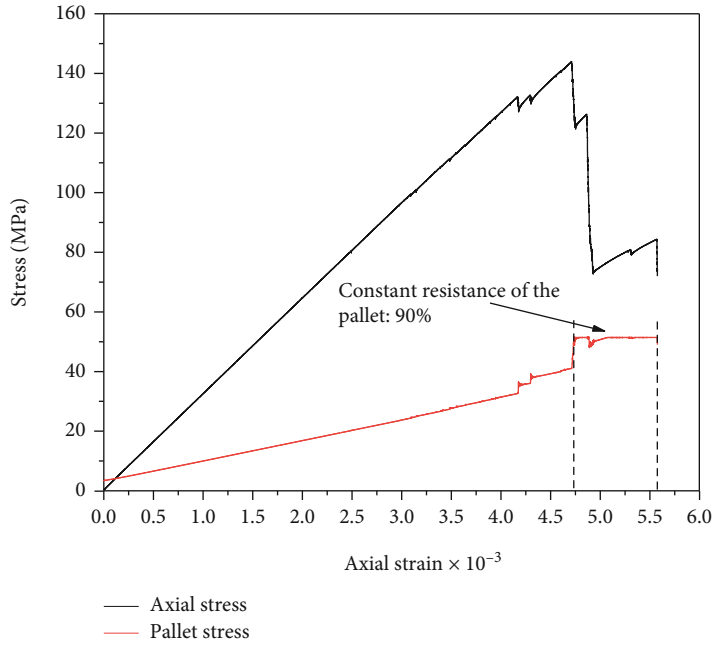

(j) R90

Figure 12: Continued.

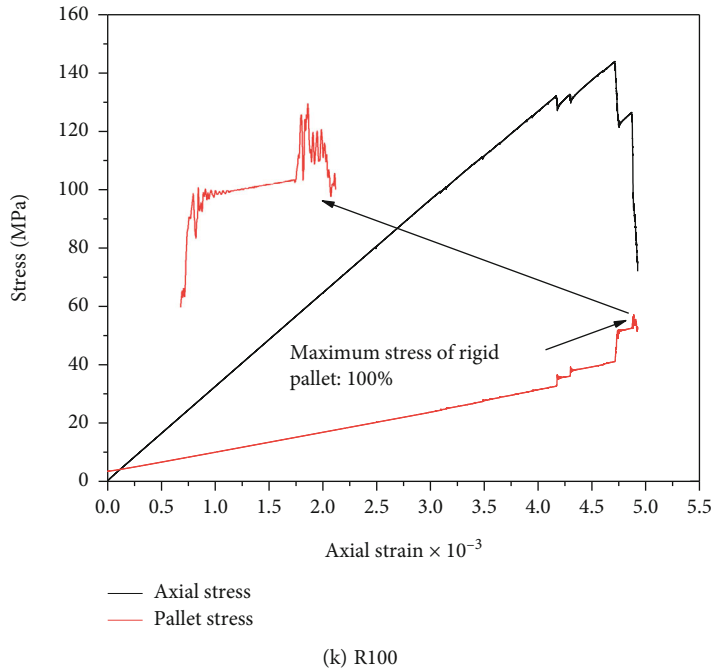

(k) R100

Figure 12: Stress-strain curve of rock sample and pallet.

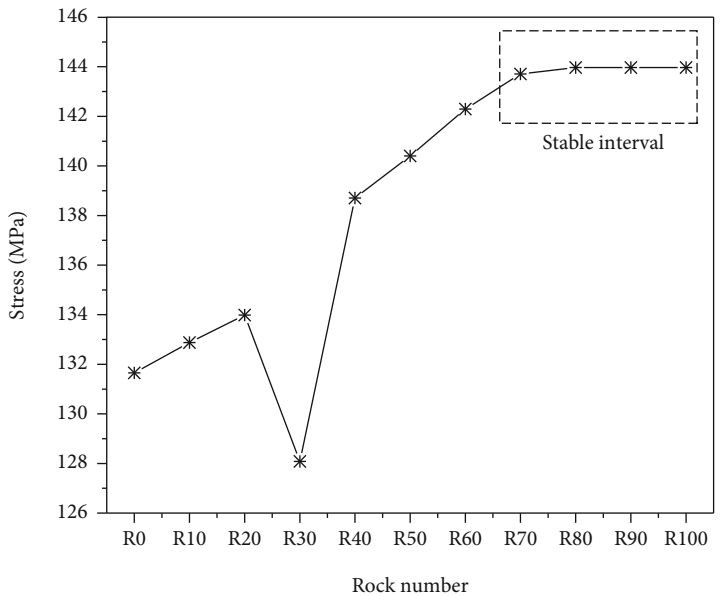

Figure 13: Strength-CRV curve.

effectively reduce the volume of the collapsed area of the surrounding rock when it has a low CRV.

4.3. Force and Displacement Field. For reflecting the impact of all CRVs on all samples, the samples at the end of the test are considered the research objects, and the force and displacement fields are shown in Figure 20.

When the CRV was greater than or equal to 30%, the force and displacement fields between the samples were basically the same. Therefore, sample R30 represents all subsequent samples. When there is no pallet, after the sample is broken, stress is mainly applied to the middle part, and the stress is more concentrated. With the appearance and increase in the CRV, the force range of the middle part gradually increases. When the CRV reaches 30%, the stress is mainly applied to the broken end, and the force range decreases again. From this perspective, it seems that a 20% CRV is more conducive to eliminating the stress

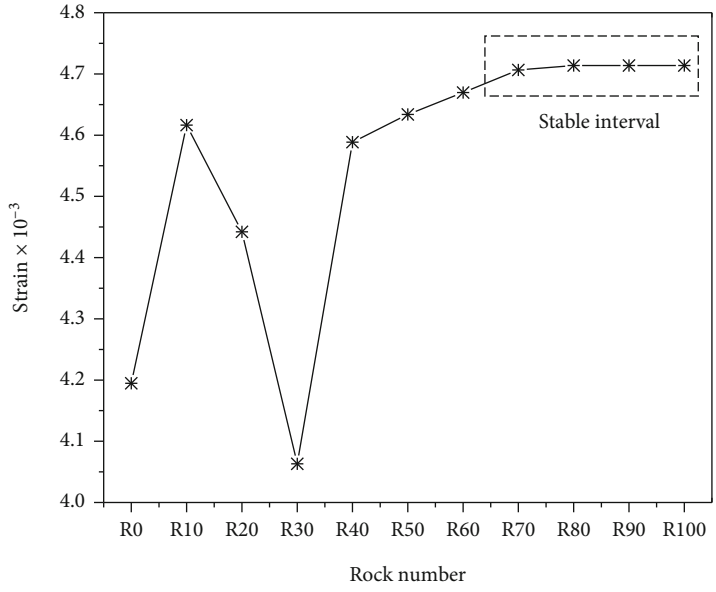

Figure 14: Peak strain-CRV curve.

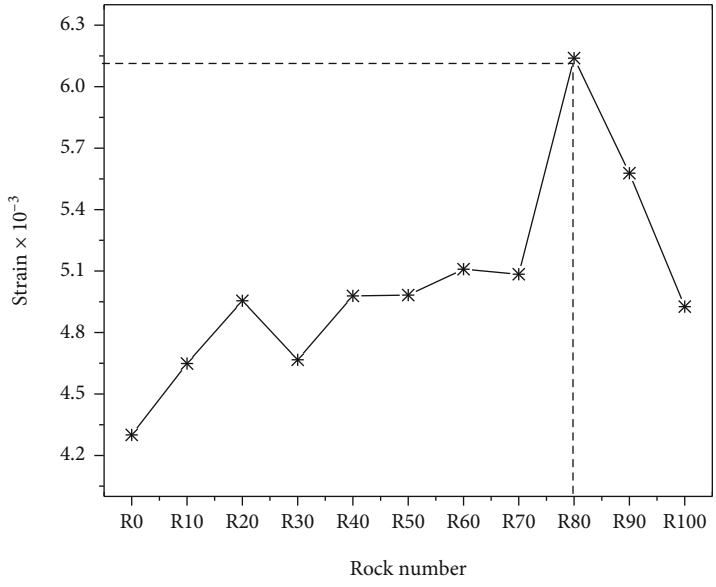

Figure 15: Maximum strain-CRV curve.

concentration phenomenon after rock failure compared to other CRVs, but notably, the test termination condition is not the final failure pattern of the surrounding rock in the actual project. As the pressure and deformation continued to increase, rock samples R10 and R20 were likely to eventually become the failure pattern of the R0 rock sample. From this perspective, a CRV greater than 30% is more beneficial to the rock.

Based on the analysis and classification method of the study [26, 27], according to the force field and combining the four displacement vector diagrams of the sample particles at the end of the test, four corresponding failure patterns are proposed: type *I*, overall single-arch caving type; type II, connected double-arch collapse type; type III, nonconnected double-arch collapse type; and type IV, local single-arch collapse type.

5. Energy Evolution Behavior

The CR cable not only has the strength of an ordinary anchor cable but also has the effect of energy absorption. For the numerical experiment in this study, the main focus

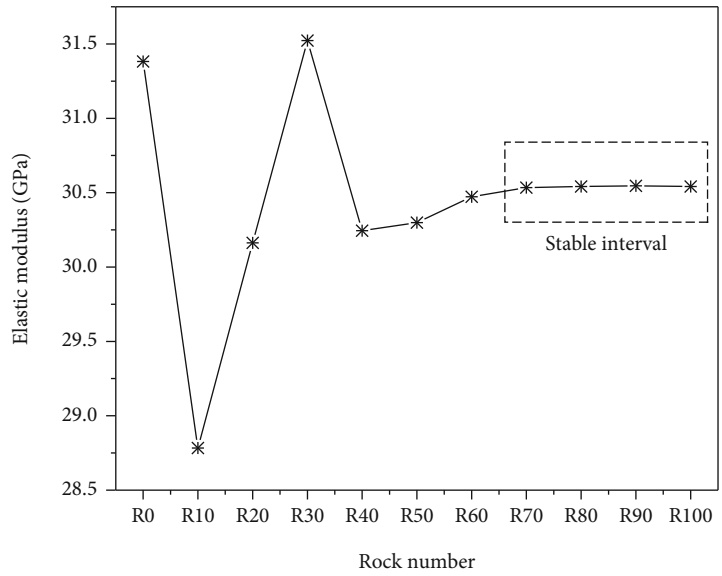

Figure 16: Elastic modulus-CRV curve.

was the energy absorption effect of pallets corresponding to different CRVs. The energy absorbed by the pallets can be expressed as

$$E = \int_0^{x_0} A\sigma x dx, \tag{4}$$

where x_0 denotes the final displacement of the pallet, A denotes the area of the pallet, σ denotes the stress variable of the pallet, and x denotes the displacement variable of the pallet.

Because A is a constant, formula (4) can be expressed as follows:

$$E_0 = \int_0^{x_0} \sigma x dx, \tag{5}$$

where E_0 was defined as the energy absorption density of the pallet. At this time, the value of E_0 is the area enclosed by the pallet's stress-displacement curve and the horizontal axis. The area can be calculated by Origin software to obtain the energy absorption density of the pallet at the end of the test and obtain the curve of the energy absorption density of the pallet with CRV (Figure 21). There are two peaks in the energy density curve: one is 10% CRV, and the other is 80% CRV. Although the energy absorption density of the R80 pallet is less than R10, the difference between the two is not large. At the same time, combined with the discussion on the best CRV in this paper, from the perspective of energy absorption, it can also be considered that 70%-80% of CRV has the best energy absorption effect.

When the pallet absorbs energy, it inevitably causes a release of strain energy inside the rock mass. Of course, the two are not equal, because the energy absorbed by the pallet can also be expressed by the following formula:

$$E = W_1 + W_2 - E_Q - \bar{E}_k, \tag{6}$$

where W_1 and W_2 are the work performed by the radial and tangential rocks of the tunnel section to the CR-anchored rock, respectively, E_Q is the heat energy, and $\bar{E}_k$ is the remaining strain energy in the CR.

In this paper, the strain energy is mainly stored in the parallel bond, as expressed by the following formula [24]:

$$\bar{E}_k = \frac{1}{2}\left(\frac{\bar{F}_n^2}{\bar{k}_n \bar{A}} + \frac{\left\|\bar{\mathbf{F}}_\mathbf{s}\right\|^2}{\bar{k}_s \bar{A}} + \frac{\left\|\bar{\mathbf{M}}_\mathbf{b}\right\|^2}{\bar{k}_n \bar{I}}\right), \tag{7}$$

where $\bar{F}_n$ denotes the normal force, $\bar{k}_n$ denotes the normal stiffness, $\bar{\mathbf{F}}_\mathbf{s}$ denotes the shear force, $\bar{k}_s$ denotes the shear stiffness, $\bar{\mathbf{M}}_\mathbf{b}$ denotes the moment of the parallel key, $\bar{A}$ is the contact area of the parallel key, and $\bar{I}$ is the moment of inertia of the contact surface.

According to (7), the final content of the parallel bond strain energy of the samples corresponding to different CRVs (Figure 22) is obtained.

On the one hand, the strain energy content in the rock is much smaller than the energy absorbed by the pallet. On the other hand, with a continuous decrease in the CRV, the strain energy of the sample also shows a monotonous decreasing trend. The lowest strain energy in the sample does not reflect the best energy absorption effect of the pallet or the best CRV, but it can reflect the energy absorption effect of the constant resistance principle on the rock to a certain extent. That is, the lower the CRV, the lower the strain energy contained in the rock when it fails. Combining the trend of the strain energy density of the pallet aforementioned, a reasonable conclusion is that a CRV of approximately 70%-80% is the best CRV, which can effectively absorb the work performed by the deformation of the

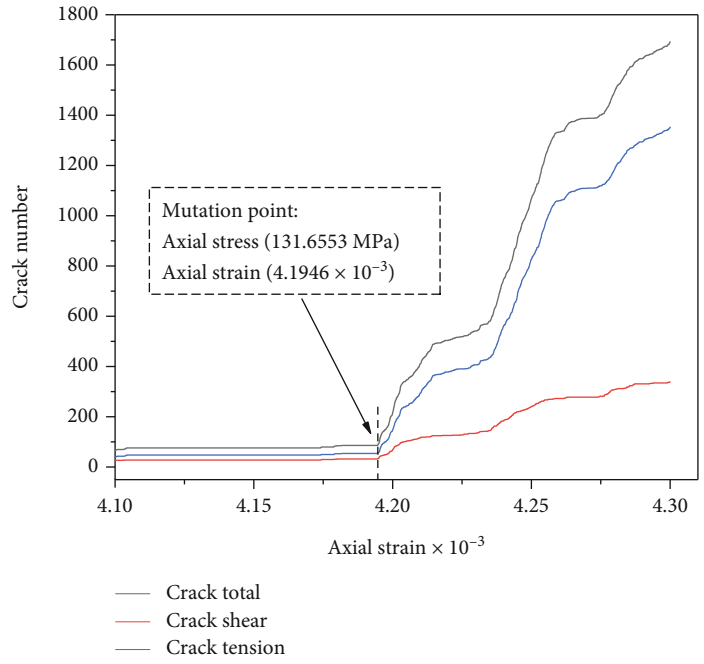

(a) R0

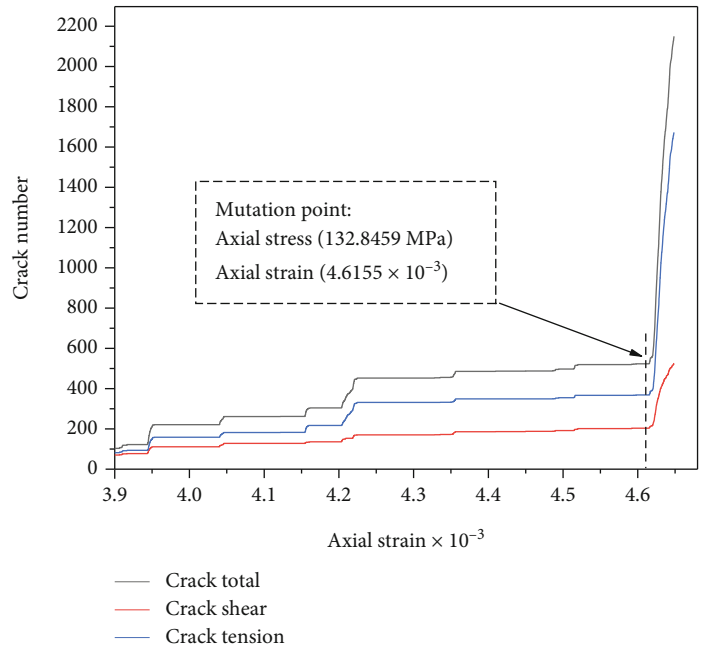

(b) R10

Figure 17: Continued.

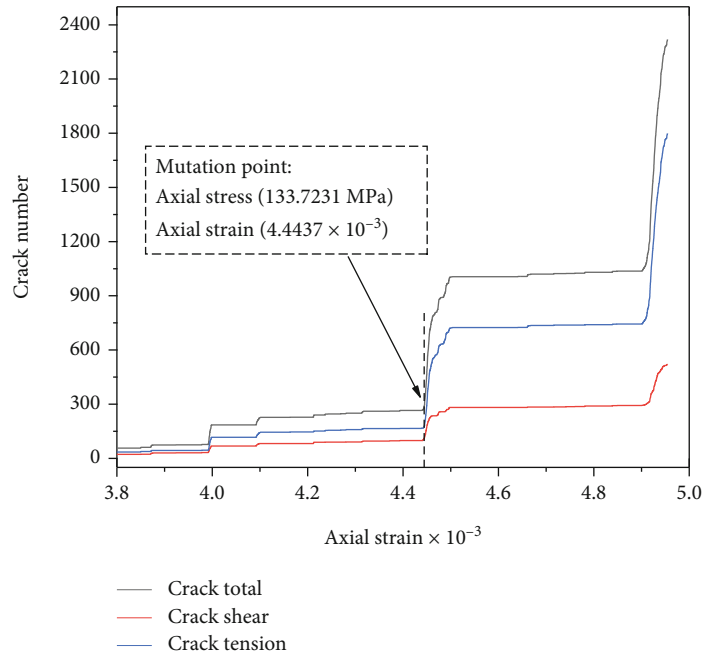

(c) R20

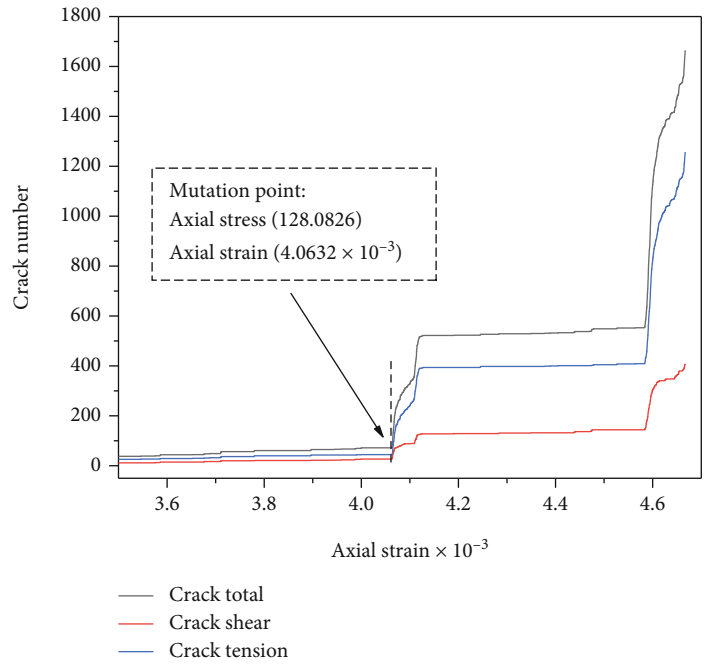

(d) R30

Figure 17: Continued.

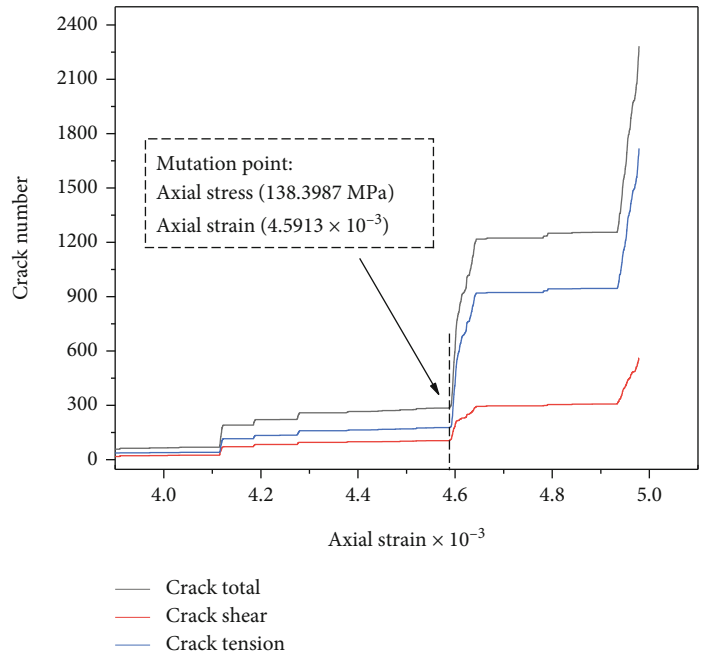

(e) R40

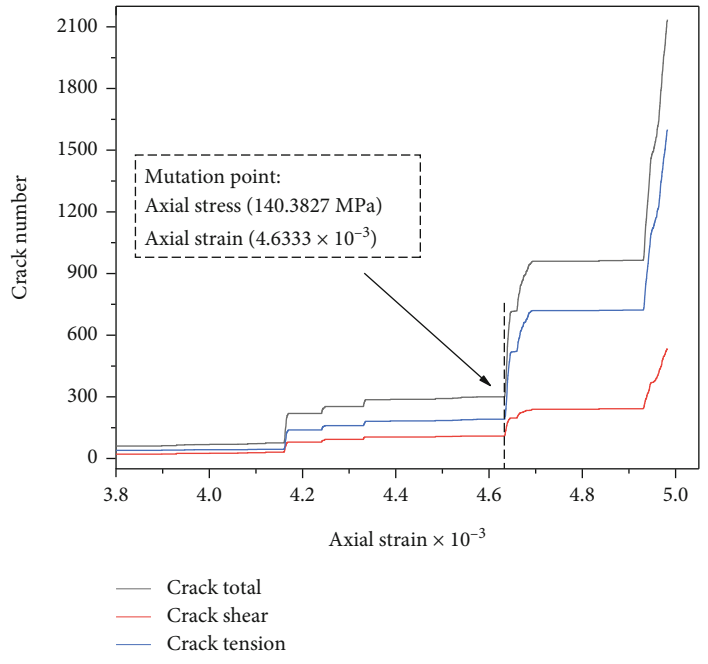

(f) R50

Figure 17: Continued.

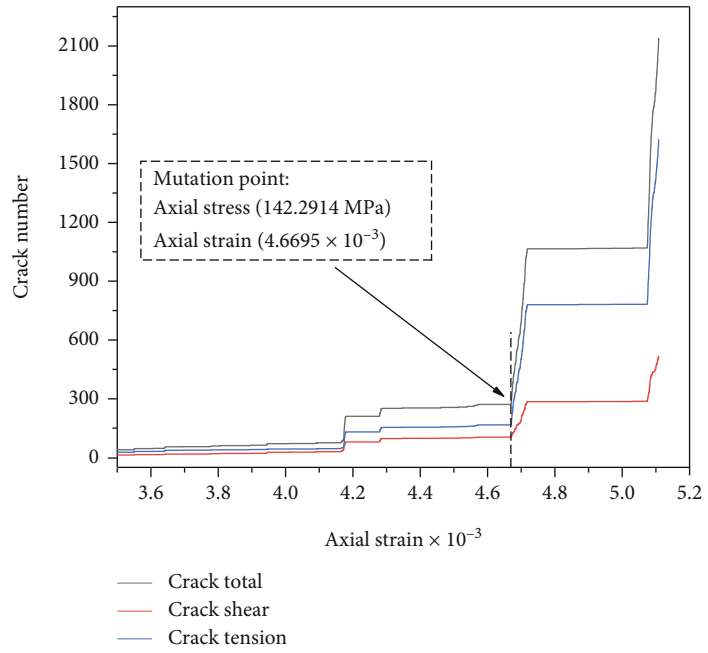

(g) R60

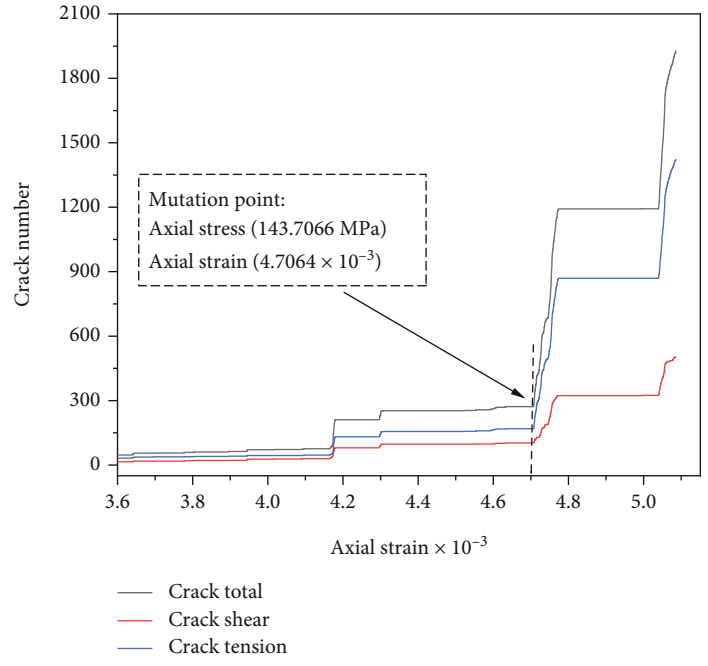

(h) R70

Figure 17: Continued.

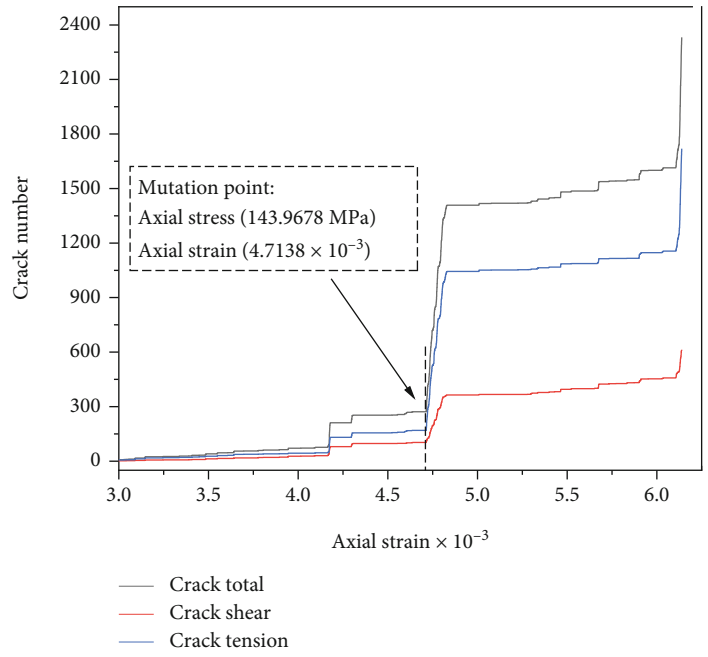

(i) R80

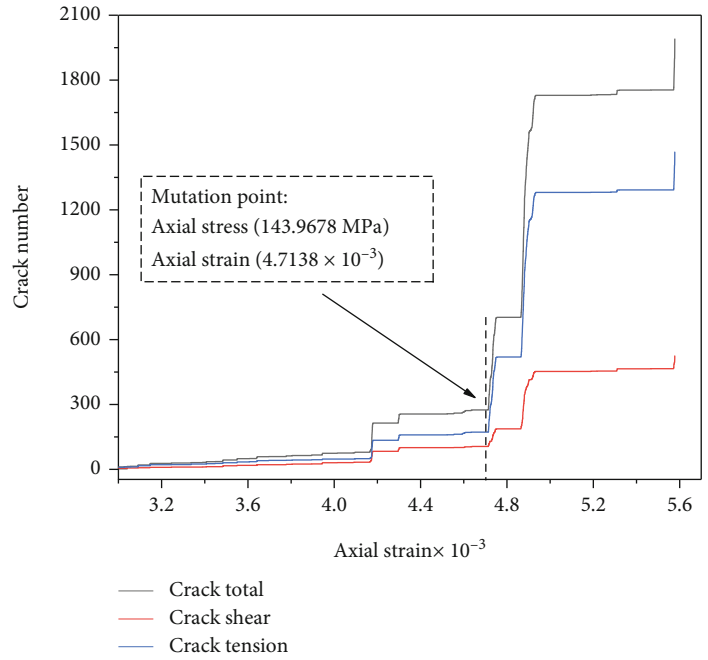

(j) R90

Figure 17: Continued.

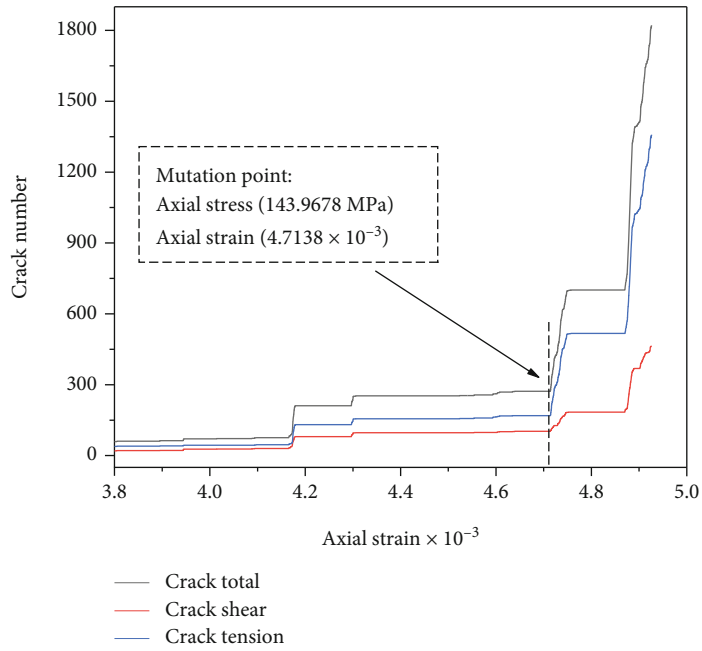

(k) R100

Figure 17: Crack number evolution curve.

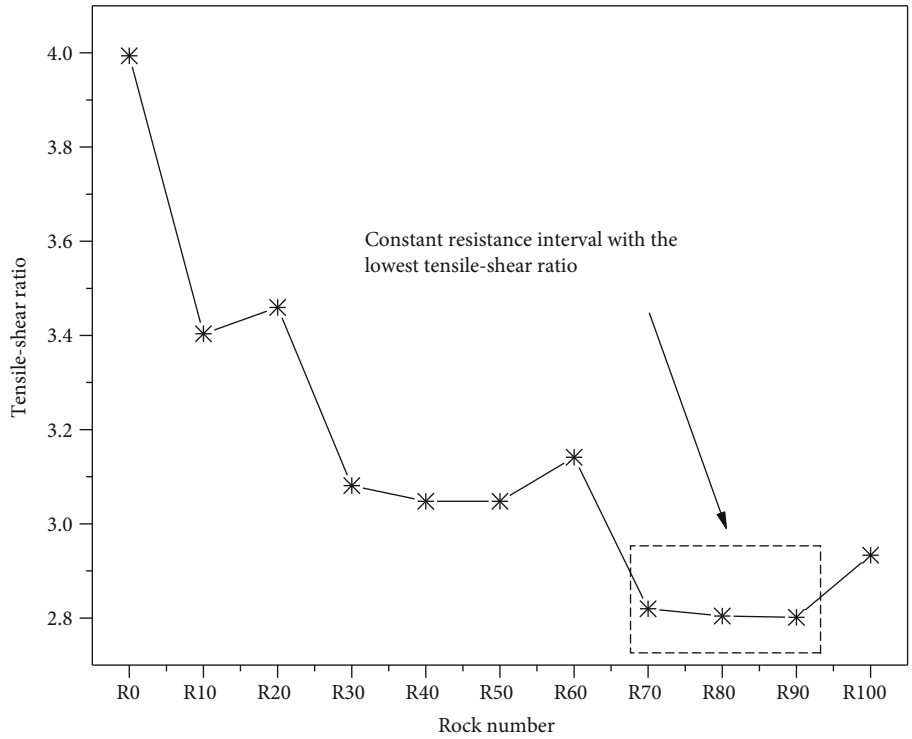

Figure 18: Ratio of tensile and shear cracks.

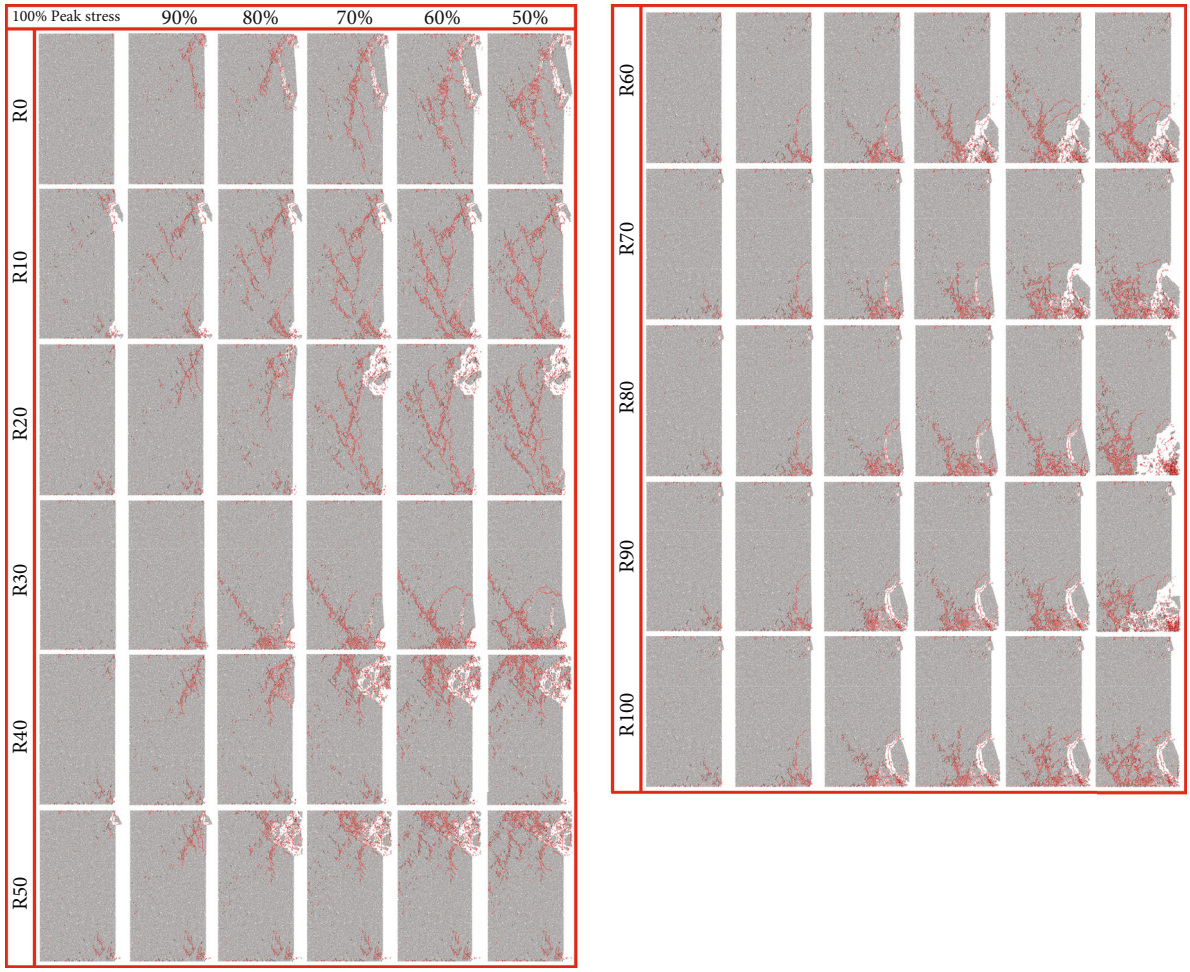

Figure 19: Crack evolution behavior corresponding to different CRVs.

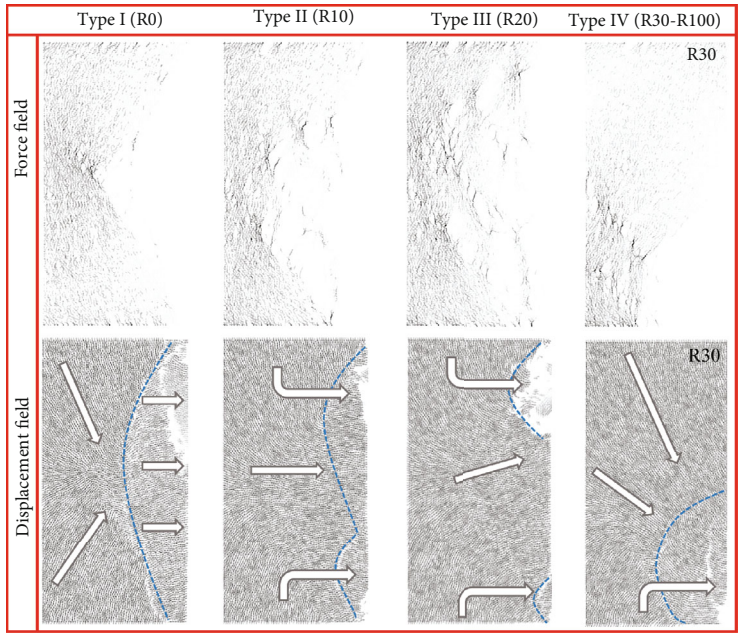

Figure 20: Four types of force and displacement field corresponding to different CRVs.

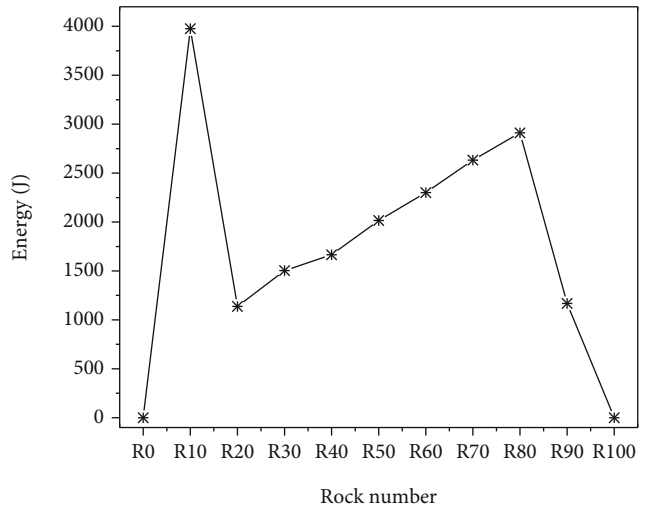

Figure 21: Pallet energy absorption density corresponding to different CRVs.

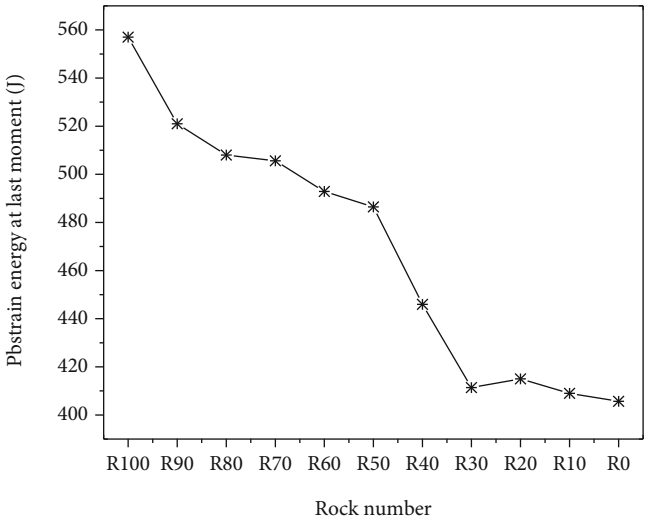

Figure 22: Strain energy contained in the sample at the end of the experiment.

surrounding rock and reduce the strain energy contained inside the rock mass when it fails.

6. Conclusion

(i) The compressive strength curve of CR-anchored rock has obvious "double peak effect." During the failure process of CR-anchored rock, there is also a "step effect" in the development of the number of cracks, and two sudden changes in the number of cracks correspond to two peaks of compressive strength

(ii) Relative to the absolute rigid cable, there is the best CRV, which is approximately 70%-80% of the supporting strength of the rigid cable when the rock fails. Within this range of CRV, the compressive strength of the rock is maximized, the deformation characteristics are relatively stable, the number ratio of tensile and shear cracks is the lowest, and the energy absorption effect of the pallet is the best, which greatly improves the strength and stability of the rock

(iii) With the continuous increase in CRV, the failure types of CR-anchored rock can be divided into four types: type *I*, overall single-arch caving type; type II, connected double-arch collapse type; type III, non-connected double-arch collapse type; and type IV, local single-arch collapse type

Data Availability

The data used to support the findings of this study are included within the article.

Conflicts of Interest

The authors declare that they have no conflicts of interest.

Acknowledgments

This work is supported by the National Natural Science Foundation of China (grant nos. 52174096 and 51874311).

References

[1] E. Gamboa and A. Atrens, "A Environmental influence on the stress corrosion cracking of rock bolts," *Engineering Failure Analysis*, vol. 10, no. 5, pp. 521–558, 2003.

[2] G. Grasselli, "3D Behaviour of bolted rock joints: experimental and numerical study," *International Journal of Rock Mechanics and Mining Sciences*, vol. 42, no. 1, pp. 13–24, 2005.

[3] Y. Cai, T. Esaki, and Y. Jiang, "An analytical model to predict axial load in grouted rock bolt for soft rock tunnelling," *Tunnelling and Underground Space Technology*, vol. 19, no. 6, pp. 607–618, 2004.

[4] Y. Wang, Z. Y. Song, T. Q. Mao, and C. Zhu, "Macro–meso fracture and instability behaviors of hollow-cylinder granite containing fissures subjected to freeze–thaw–fatigue loads," *Rock Mechanics and Rock Engineering*, vol. 55, no. 7, pp. 4051–4071, 2022.

[5] C. C. Li, "Field observations of rock bolts in high stress rock masses," *Rock Mechanics and Rock Engineering*, vol. 43, no. 4, pp. 491–496, 2010.

[6] X. F. Deng, J. B. Zhu, S. G. Chen, Z. Y. Zhao, Y. X. Zhou, and J. Zhao, "Numerical study on tunnel damage subject to blast-induced shock wave in jointed rock masses," *Tunnelling and Underground Space Technology*, vol. 43, pp. 88–100, 2014.

[7] C. S. Zhang, D. H. Zou, and V. Madenga, "Numerical simulation of wave propagation in grouted rock bolts and the effects of mesh density and wave frequency," *International Journal of Rock Mechanics and Mining Sciences*, vol. 43, no. 4, pp. 634–639, 2006.

[8] H. P. Kang, Y. Z. Wu, F. Q. Gao, J. Lin, and P. F. Jiang, "Fracture characteristics in rock bolts in underground coal mine roadways," *International Journal of Rock Mechanics and Mining Sciences*, vol. 62, pp. 105–112, 2013.

[9] Y. Wang, J. Z. Li, C. Zhu, and T. Mao, "Fatigue failure identification using deformation and energy rate for hole- fissure contained granite under freeze–thaw and variable-frequency–variable-amplitude cyclic loads," *Fatigue & Fracture of Engineering Materials & Structures*, vol. 45, no. 3, pp. 834–851, 2022.

[10] J. D. Yu, M. H. Bae, S. I. Han, I. M. Lee, and J. S. Lee, "Defect ratio evaluation of the rock bolt grouting using the reflection method of guided ultrasonic waves," *Journal of Korean Tunnelling and Underground Space Association*, vol. 10, pp. 221–232, 2008.

[11] V. Deodeshmukh, A. Venugopal, D. Chandra et al., "X-ray photoelectron spectroscopic analyses of corrosion products formed on rock bolt carbon steel in chloride media with bicarbonate and silicate ions," *Corrosion Science*, vol. 46, no. 11, pp. 2629–2649, 2004.

[12] T. Zhou, J. B. Zhu, Y. Ju, and H. P. Xie, "Volumetric fracturing behavior of 3D printed artificial rocks containing single and double 3D internal flaws under static uniaxial compression," *Engineering Fracture Mechanics*, vol. 205, pp. 190–204, 2019.

[13] M. He, W. Gong, J. Wang et al., "Development of a novel energy-absorbing bolt with extraordinarily large elongation and constant resistance," *International Journal of Rock Mechanics and Mining Sciences*, vol. 67, pp. 29–42, 2014.

[14] M. C. He and Z. B. Guo, "Mechanical property and engineering application of anchor bolt with constant resistance and large deformation," *Chinese Journal of Rock Mechanics and Engineering*, vol. 33, pp. 1297–1308, 2014.

[15] M. C. He and W. L. Gong, "Support principles of NPR bolts/cables and control techniques of large deformation," *Chinese Journal of Rock Mechanics and Engineering*, vol. 35, pp. 1514–1529, 2016.

[16] Z. Tao, Y. Wang, C. Zhu, H. Xu, G. Li, and M. He, "Mechanical evolution of constant resistance and large deformation anchor cables and their application in landslide monitoring," *Bulletin of Engineering Geology and the Environment*, vol. 78, no. 7, pp. 4787–4803, 2019.

[17] J. Hu, Z. Li, and J. Feng, "Analytical model of elasto-plastic and numeric analysis for the constant resistance large deformation(NPR) cable," *Chinese Journal of Rock Mechanics and Engineering*, vol. 38, no. S2, pp. 3565–3574, 2019.

[18] Y. Wang, T. Mao, Y. Xia, X. Li, and X. Yi, "Macro-meso fatigue failure of bimrocks with various block content subjected to multistage fatigue triaxial loads," *International Journal of Fatigue*, vol. 163, p. 107014, 2022.

[19] Z. Li, Q. Lv, H. Zhu, J. Hu, J. Feng, and M. He, "Laboratory testing and modeling of a high-displacement cable bolt," *International Journal of Geomechanics*, vol. 19, pp. 1943–5622, 2019.

[20] Z. Li, Y. Jiang, Z. Tao, and M. He, "Monitoring prediction of a rockslide in an open-pit mine and numerical analysis using a material instability criterion," *Bulletin of Engineering Geology and the Environment*, vol. 78, no. 3, pp. 2041–2053, 2019.

[21] M. He, C. Li, W. Gong, L. R. Sousa, and S. Li, "Dynamic tests for a constant-resistance-large-deformation bolt using a modified SHTB system," *Tunnelling and Underground Space Technology*, vol. 64, pp. 103–116, 2017.

[22] Y. Wang, J. Han, Y. Xia, and D. Long, "New insights into the fracture evolution and instability warning predication for fissure-contained hollow-cylinder granite with different hole diameter under multi-stage cyclic loads," *Theoretical and Applied Fracture Mechanics*, vol. 119, p. 103363, 2022.

[23] M. Bahaaddini, G. Sharrock, and B. K. Hebblewhite, "Numerical direct shear tests to model the shear behaviour of rock joints," *Computers and Geotechnics*, vol. 51, pp. 101–115, 2013.

[24] Itasca, *Particle Flow Code 2D, version 6.0*, Itasca Consulting Group, Inc., 2018.

[25] H. Shi, H. Zhang, L. Song et al., "Failure characteristics of sandstone specimens with randomly distributed pre-cracks under uniaxial compression," *Environmental Earth Sciences*, vol. 79, no. 9, pp. 1–21, 2020.

[26] Y. H. Huang, S. Q. Yang, P. G. Ranjith, and J. Zhao, "Strength failure behavior and crack evolution mechanism of granite containing pre-existing non-coplanar holes: experimental study and particle flow modeling," *Computers and Geotechnics*, vol. 88, pp. 182–198, 2017.

[27] J. Jin, P. Cao, Y. Chen, C. Pu, D. Mao, and X. Fan, "Influence of single flaw on the failure process and energy mechanics of rock-like material," *Computers and Geotechnics*, vol. 86, pp. 150–162, 2017.